APPLIED PHYSICS

Climbing droplets driven by mechanowetting on transverse waves

Edwin De Jong[1], Ye Wang[2], Jaap M. J. Den Toonder[2], Patrick R. Onck[1]*

Many applications in modern technology, such as self-cleaning surfaces and digital microfluidics, require control over individual fluid droplets on flat surfaces. Existing techniques may suffer from side effects resulting from high electric fields and high temperatures. Here, we introduce a markedly different method, termed "mechanowetting," that is based on the surface tension–controlled droplet motion on deforming surfaces. The method is demonstrated by transporting droplets using transverse surface waves on horizontal and (vertically) inclined surfaces at transport velocities equal to the wave speed. We fully capture the fundamental mechanism of the mechanowetting force numerically and theoretically and establish its dependence on the fluid properties, surface energy, and wave parameters. Mechanowetting has the potential to lead to a range of new applications that feature droplet control through dynamic surface deformations.

INTRODUCTION

Many applications in modern technology, such as self-cleaning surfaces (*1*) and digital microfluidics (*2*–*5*), require control over fluid droplets that need to be moved, merged, split, or mixed on surfaces. Existing droplet manipulation technologies can have some serious drawbacks, such as field-induced sample disturbance and complex electrode patterns in case of electrowetting (*6*–*8*), high temperatures in Leidenfrost propulsion (*9*, *10*), small velocities in molecular motor-driven transport (*11*), need for piezoelectric substrates and integrated patterned electrodes for surface acoustic waves (*12*–*14*), and limited flexibility of static wetting gradients (*15*). Here, we show that these drawbacks may be overcome by controlling the movement of individual droplets through "mechanowetting," the dynamic manifestation of three-phase line pinning to deforming surface topographies. The mechanism is demonstrated by transporting droplets using transverse surface waves on horizontal and inclined surfaces at transport velocities equal to the speed of the wave. We quantify the dynamic pinning force that drives mechanowetting by studying climbing droplets of different sizes at varying inclination angles. The forces are unexpectedly large and able to drive droplets even against vertical walls at substantial droplet speeds. It is shown that contaminating particles can be picked up by the droplets, demonstrating the potential of mechanowetting for self-cleaning surfaces. We fully capture the fundamental mechanism underlying droplet transport numerically and theoretically and establish its dependence on the fluid properties, surface energy, and wave parameters. We expect mechanowetting to lead to a wide range of new applications based on three-phase line manipulation by switchable surface topographies.

RESULTS AND DISCUSSION

To experimentally demonstrate droplet transport, we built a device that generates regular and controllable transverse surface waves (Fig. 1A). By lowering the pressure underneath the film, a 50-μm-thick polydimethylsiloxane (PDMS) film is pressed against a moving belt with transversely aligned ridges, creating a wave-like surface structure. The edge of the film is clamped by a static metal frame, horizontally constraining the film so that it can make no translational movement, ensuring that the wave is purely transverse. The wavelength λ of the film is determined by the spacing of the ridges on the belt, and the wave amplitude A is controlled by the vacuum pressure, with typical values between 3 and 5 μm (for details, see Materials and Methods). Individual droplets with volumes in the range 0.1 to 5 μl on transverse waves with wavelength λ = 500 μm were found to be traveling at a speed of 0.57 mm s^{-1}, equal to the applied wave speed. Figure 1 (B to D) shows three snapshots during transport (see movie S1) of a 1.3-μl droplet.

To quantify the driving force, explore the fundamental physical mechanisms, and optimize the response of the system, we carried out a combination of computational fluid dynamics (CFD) simulations, theoretical modeling, and single-droplet experiments. We numerically analyzed individual droplets using a CFD model with vertically deforming boundaries, which was developed within the OpenFOAM framework (*16*–*20*). Figure 1 (E to G) shows three snapshots of a simulation (see movie S2) for a 1.4-μl droplet, showing excellent agreement with the experiments (Fig. 1, B to G). By tracking the particles inside the droplet (Fig. 1, B to D) and comparing them to the internal droplet velocity in the CFD simulations (Fig. 1, E to G), we observe a rotational, treadmill-like flow pattern during transport. This observation becomes especially apparent in the superposed image in fig. S1, where the particle locations are used to generate the path lines.

To probe the effectiveness of the droplet transportation mechanism, we carried out a series of "climbing droplet" experiments and simulations. During the droplet transportation experiments, the device was slowly tilted at an increasing angle β (see the inset of Fig. 2A) until, at a critical angle β_{crit}, the gravitational force became larger than the driving force of droplet transportation, resulting in the droplet to slide off. We carried out multiple experiments for droplets of different volume V and recorded the critical angles β_{crit}. This critical angle is plotted in Fig. 2A as a function of the normalized droplet size d/λ, with d as the diameter of the droplet contact area, which depends on both volume and contact angle (see Materials and Methods), and λ as the wavelength. The graph shows a clear overall trend that β_{crit} decreases with an increase in droplet size. This is expected because the gravitational force increases faster ($\sim d^3$) than the droplet driving

[1]Zernike Institute for Advanced Materials, University of Groningen, Groningen 9747 AG, Netherlands. [2]Department of Mechanical Engineering and Institute for Complex Molecular Systems, Eindhoven University of Technology, Eindhoven 5600 MB, Netherlands.
*Corresponding author. Email: p.r.onck@rug.nl

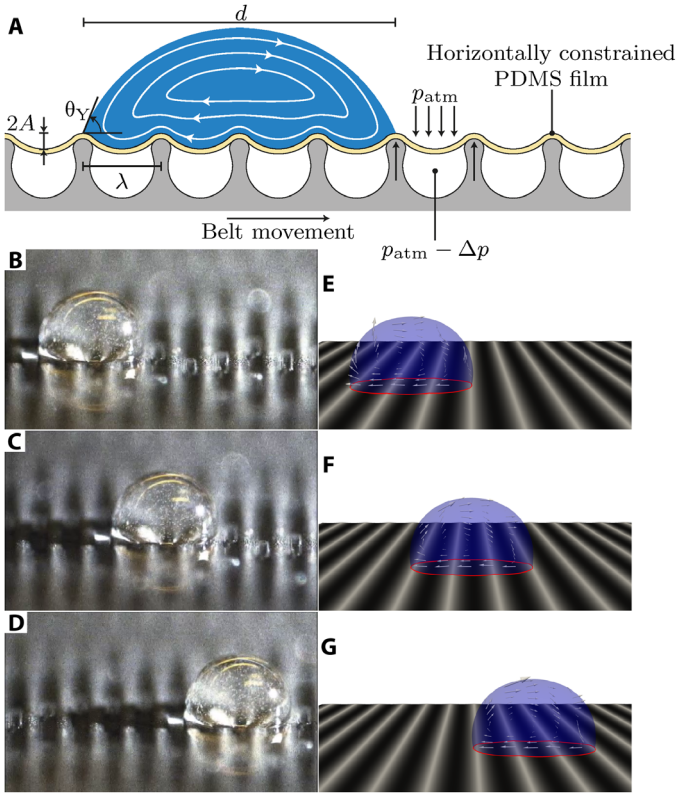

Fig. 1. Droplet transport on transverse wave surface topographies. (**A**) Schematic of the experimental setup of the transverse wave device. Here, A is the wave amplitude, λ is the wavelength, θ_Y is the contact angle, d is the typical droplet size, p_{atm} is the atmospheric pressure, and Δp is the pressure difference created by a vacuum pump to transform the flat PDMS film into a wave-like surface structure with a wavelength that is dictated by the ridge spacing of the belt. The streamlines inside the droplet are a schematic to illustrate the internal droplet flow in the center-of-mass frame following the droplet. (**B** to **D**) Glycerol droplet containing tracer particles transported by the traveling wave device (see movie S1). Here, $A = 4 \pm 1$ μm, $\lambda = 500$ μm, and $\theta_Y = 100 \pm 2°$. In fig. S1, the frames of the movie are superposed to generate path lines, demonstrating the treadmill-like internal flow pattern consistent with Fig. 1A. (**E** to **G**) Computational fluid dynamics (CFD) simulations of the glycerol droplet on a transversely deforming surface boundary for the same traveling wave characteristics (shape, wave amplitude, wave speed, and wavelength), droplet properties, and Young angle as in the experiments (see Materials and Methods and movie S2). The small arrows inside the droplet indicate the local fluid velocity in the center-of-mass reference frame.

force that acts through the three-phase contact line (~d). It can also be observed from Fig. 2A that β_{crit} does not decrease monotonically but exhibits local maxima close to integer values of d/λ. In Fig. 2 (B and C) and movie S3, we demonstrate this effect by placing two droplets of different sizes on the traveling wave inclined at 13° (indicated by the dashed lines in Fig. 2A). The driving force for the bigger droplet ($d/\lambda = 3.1$) is larger than the gravitational force (conforming with Fig. 2A) so that the droplet climbs upward ($\beta < \beta_{crit}$). In contrast, the driving force for the smaller droplet ($d/\lambda = 2.7$) is smaller than the gravitational force so that the droplet slides down ($\beta > \beta_{crit}$).

The material and transverse wave input parameters for the simulations were set equal to the experimental values (see Materials and Methods and the caption of Fig. 2A). The CFD model is found to capture the alternating trend of the critical angle in the experiments very accurately. Here, the transparent area in orange shows the error margin that was introduced by the variation of the wave amplitude on the traveling wave device (±1.0 μm) and the solid line corresponds to A = 4.0 μm. To further explore the effect of the surface parameters on the transport mechanism, we used the CFD model to investigate the influence of the wave speed and amplitude on the critical angle. The results in Fig. 2D show that the critical angle decreases by increasing the wave speed, and it was found that, for high wave speeds at the lower range of amplitudes, the driving force was insufficient to generate droplet transport. This is due to an enhanced viscous drag related to an increase in viscous dissipation inside the droplet. The correlation between dissipation and droplet speed is caused by the fact that a larger transport speed of the droplet necessarily leads to larger flow velocities inside the droplet due to the treadmill-like nature of droplet transport (see Fig. 1). In addition, an increasing wave amplitude was found to (linearly) increase β_{crit}. This consistent increase of transport efficiency with wave amplitude is a very powerful asset of this transport mechanism, allowing it to overcome retardation forces that may originate from contact angle hysteresis and viscous effects.

To explore the oscillatory nature of β_{crit} in Fig. 2A, we analyzed the shape of the droplets and their contact line during transportation using CFD. We focused on two different droplet sizes: $d/\lambda = 2.1$ for which β_{crit} attains a maximum [shown in Fig. 3 (A and B), top row] and $d/\lambda = 2.7$ for which β_{crit} attains a minimum [in Fig. 3 (C and D, top row]. The droplets at zero inclination and wave speed (Fig. 3, A and C) attain a symmetric shape. Once the wave starts moving and the device is tilted, the droplet's position with respect to the ridges is distorted and it attains an asymmetric configuration, as shown in Fig. 3 (B and D). The distortion brings the system out of equilibrium, which triggers a restoring force that drives droplet motion. To quantify this restoring force, we developed a theoretical model based on the instantaneous change of the local contact angle when the droplet is distorted. By modeling the droplet as a spherical cap and capturing the amount of droplet distortion in a (phase) shift of the droplet's center of mass with respect to the equilibrium position on the traveling wave, we calculated the resulting force per unit length (i.e., tension) originating from the unbalance of the surface tension forces at the contact line (see Supplementary Text, "Three-phase line integral theory"). These tensions correspond to the blue arrows at the bottom of Fig. 3. The total force is obtained by integrating the tensions along the three-phase line, resulting in a net force represented by the red arrow in the center of the drop. The theoretical approach confirms that, in the equilibrium positions (Fig. 3, A and C), the three-phase line tensions are symmetric, while the distorted droplets show a clear asymmetry, generating a net force in the positive x direction, dynamically pinning the droplet to its equilibrium position (see the Supplementary Text for a detailed discussion). During droplet transport, this "dynamic-pinning force" balances the counteracting forces, such as static pinning, gravity, and viscous forces. The theory quantitatively captures the oscillatory effect in Fig. 2A (see also fig. S2) and is used to determine the dependence of the dynamic pinning force on (i) the applied phase shift (fig. S3-I, A and B), (ii) the contact angle (fig. S3-IC), and (iii) the normalized amplitude A/λ (fig. S3-ID). Last, we derived that the highest forces can be generated for contact angles near 65.5° (see Supplementary Text).

The droplets deposited on the traveling waves are able to overcome considerable gravitational forces and are even able to climb up vertically

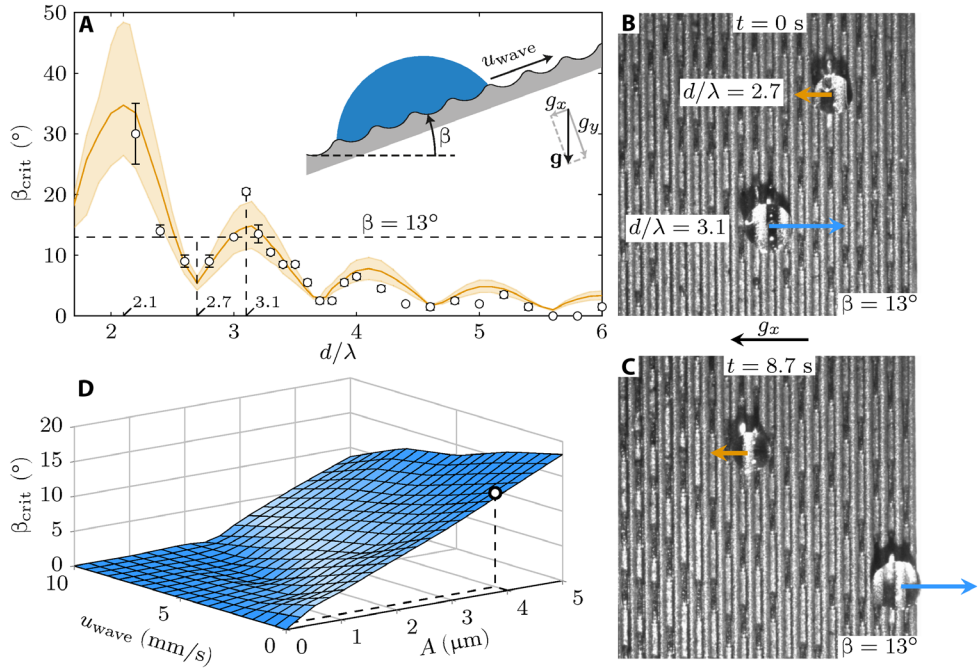

Fig. 2. Droplet transport on inclined surfaces. (**A**) Critical angle β_{crit} as a function of the droplet size d normalized by the wavelength λ (see Materials and Methods). The markers are experimental results; error bars represent the SD of at least three measurements. The trend line corresponds to numerical results. The numerical model uses the experimental settings as input, i.e., the Young angle $\theta_Y = 68°$, wavelength $\lambda = 500$ μm, amplitude $A = 4.0 \pm 1.0$ μm, and the dynamic viscosity $\nu = 1$ mm^2 s^{-1} of the fluid (water-isopropanol; see Materials and Methods). The error margin in the amplitude is reflected by the shaded area around the main trend line (in orange). (**B** and **C**) Two-droplet experiment showing droplets of size $d/\lambda = 2.7$ and 3.1 at inclination angle $\beta = 13°$ [corresponding to the marked locations in (A) indicated by the dashed lines]. The arrows indicate the droplet movement. (**D**) Numerical results depicting the change in critical angle β_{crit} as a function of wave speed u_{wave} and wave amplitude A for a droplet of size $d/\lambda = 3.2$ ($\lambda = 500$ μm). The marked data point corresponds to the amplitude and wave speed of the experiments shown in (A).

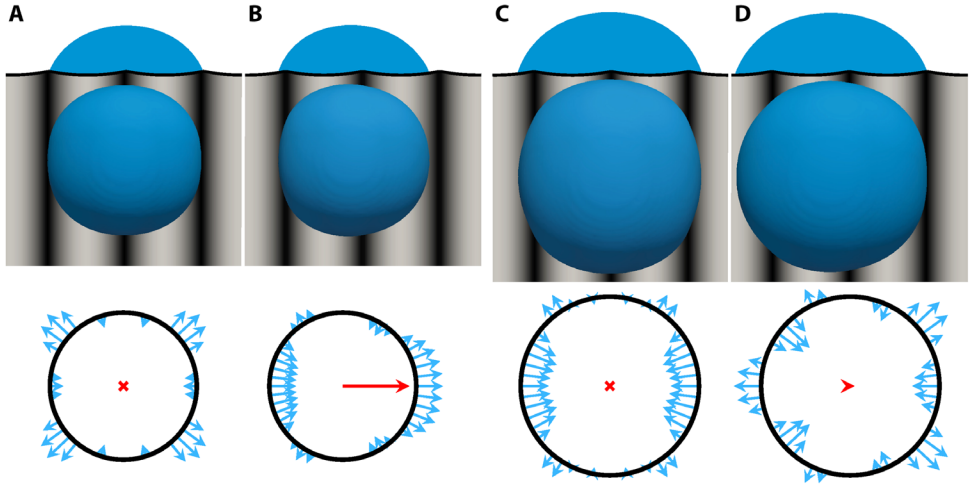

Fig. 3. Numerical and theoretical analysis of climbing droplets. The top row shows simulation snapshots (cross-sectional and top views), and the bottom row shows theoretical results from the three-phase line integral theory (see Materials and Methods) of a 0.15-μl droplet ($d/\lambda = 2.1$) (**A** and **B**) and a 0.30-μl droplet ($d/\lambda = 2.7$) (**C** and **D**) for wave amplitude $A = 5$ μm. The situations in (A) and (C) correspond to zero wave speed and inclination, $u_{wave} = 0$ mm s^{-1} and $\beta = 0$, and the situations in (B) and (D) correspond to a wave speed $u_{wave} = 0.57$ mm s^{-1} (CFD results only) and inclination angles $\beta \approx \beta_{crit} \approx 48°$ and 7°, respectively. The height of the surface ridges (top row) is indicated by a gray scale in the top view and is exaggerated in the cross-sectional view.

inclined surfaces (in the case of small droplets) at an inclination-independent velocity of 0.57 mm s^{-1} (Fig. 4A and movie S4). In addition to vertical climbing, we also demonstrate millimeter-sized droplets that are transported upside down (Fig. 4B and movie S5). This consistent uphill and inverted transport of droplets on surfaces with traveling wave topographies has, to the best of our knowledge, not been realized before. The maximal forces that our mechanowetting device has generated during the experiments presented in Fig. 2A is around

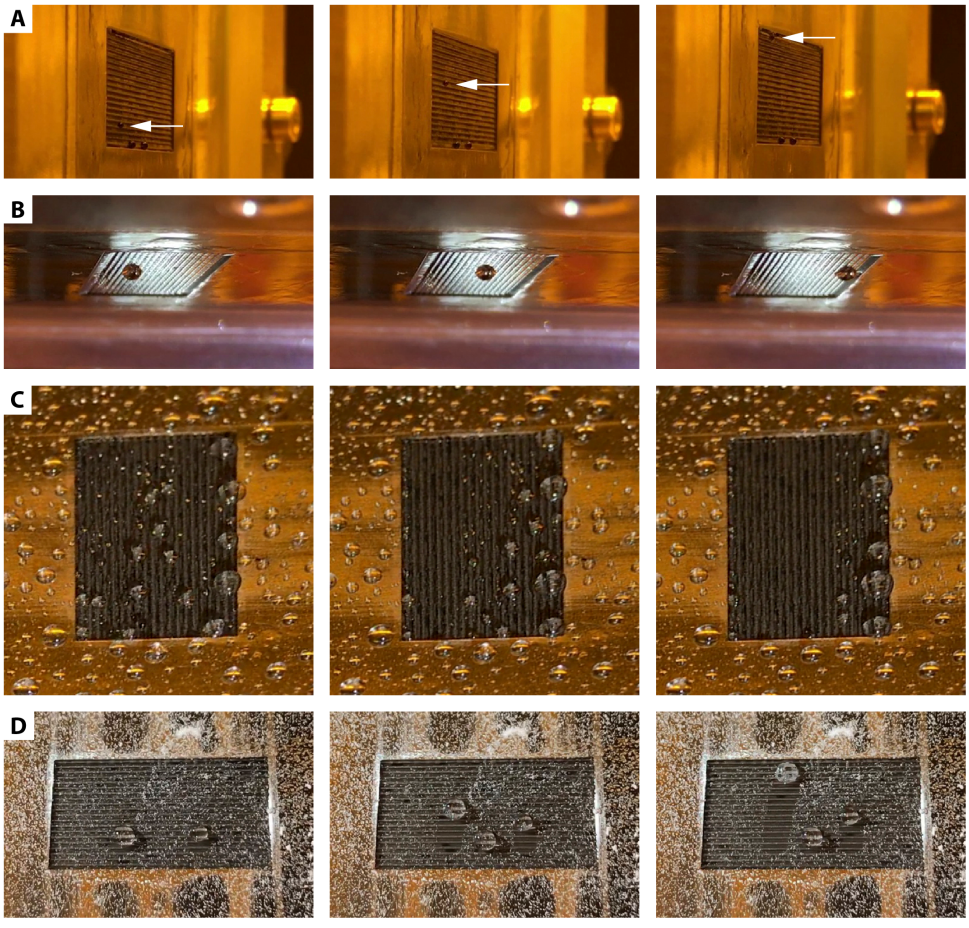

Fig. 4. Droplet transport demonstrations. (**A**) "Vertical transport," i.e., a vertically climbing water-glycerol droplet at a constant speed of 0.57 mm s^{-1} (movie S4). (**B**) "Ceiling transport," i.e., transport of a droplet (isopropanol-water mixture) at a constant speed of 0.57 mm s^{-1} on a fully reversed (upside down) surface (movie S5). (**C**) "Mass transport of multidispersed droplets," i.e., water droplets sprayed on an inclined traveling surface wave taken along with the wave (movie S6). (**D**) "Self-cleaning surface," i.e., transporting droplets picking up calcium carbonate contaminating particles (movie S7). Photo credits: (A) E.D.J. and (B to D) Y.W.

2 μN (for $d/\lambda = 5.2$, corresponding to a droplet of 4.6 μl and a surface tension γ_{LV} of 26 mN m^{-1}; see the red graph in fig. S2), which compares positively to the first-order approximation of ~0.4 μN for the maximal forces generated using tubular actuators (estimate based on transport of 0.12-μl slugs at 17° inclination angles) (*21*). The distance over which the droplet can be transported in our experiment is limited only by the size of the active area of the device. Enlarging this area will result in larger distances traveled at the same velocity. This observation emphasizes an advantage over static methods such as (chemical) wetting gradients (*22*) that are limited by the permanent pattern that is imprinted on the material, which is, by definition, finite [e.g., 1 cm in Chaudhury and Whiteside's work (*22*)]. Creating a wetting gradient that lasts over a longer distance will reduce the applied force resulting in compromised transport properties.

We have tested the method on several fluids (including water, isopropanol, and mineral oil) and found that the method is very robust, showing consistent, reproducible droplet movement for all cases tested. We demonstrate its efficiency in Fig. 4C and movie S6 by spraying a large amount of (water) droplets of multiple sizes on the traveling wave simultaneously. Here, we see that the transverse wave completely wipes the surface clean in a matter of seconds. Initially, some of the droplets are not transported, possibly due to small mechanowetting forces for that specific droplet size or local hysteresis. However, because of merging with transporting droplets their size increases, leading to an altered driving force and position and, thus, to subsequent transport. The mechanowetting principle can be applied to a very wide range of solid-fluid-vapor systems, covering almost the full range of wetting angles, with the limiting exceptions of $\theta_Y = 0°$ and 180° (see Supplementary Text and fig. S3-IC). This versatility of mechanowetting is remarkable, given the fact that other methods have special requirements, such as electrically conducting liquids and preferred large contact angles for electrowetting or the need for fully wetting solid walls to circumvent hysteresis in microchannels (*21*).

The variation in the critical angle shown in Fig. 2A allows for a new method of droplet sorting. By tilting the setup at a certain angle (e.g., the angle indicated by the dashed line in Fig. 2A), droplet sizes with a critical angle below the threshold will not be able to travel along with the wave, while droplets that exhibit larger maximum critical angles will be transported [as demonstrated for a specific situation in Fig. 2 (B and C)]. The consequence is that only droplets of certain size (i.e., above the dashed line) will travel along with the wave, while the rest will slide off the inclined surface. When two droplets coalesce, this selection process

is repeated and the droplet will be selected on the basis of its new size. These sorting principles can also be used to select droplets that have different physical properties, such as surface tension (linear scaling), contact angle ($\sin\theta_Y$ scaling), or viscosity (see Fig. 1D).

We explored the self-cleaning propensity of the constructed traveling wave surface and found that droplets deposited on the traveling surface wave are able to wipe the surface clean from surface contamination. We constructed a model "contaminated surface" by depositing a large amount of calcium carbonate particles (particle size, <50 μm; Sigma-Aldrich) on top of the PDMS film. Upon switching on the traveling wave (in the absence of droplets), the contamination particles stay at their location on the surface as expected, given the mere transverse nature of the wave. After deposition of water-isopropanol droplets of various sizes, the droplets are transported by the transverse wave and clean the surface (Fig. 4D and movie S7). Although the large particle count increased the contact angle hysteresis significantly, leading to an increase in resistance and a reduction in effective droplet velocity to 20% of the wave speed, the droplets are able to pick up the contamination particles along their path, leaving a clean trail behind. The particles are taken up in the interior of the droplets and are transported while continuously cycling around the center of mass, as shown in Fig. 1. The pickup and transport of the particles demonstrate the droplet-induced self-cleaning capability of mechanowetting surfaces. Self-cleaning superhydrophobic surfaces that consist of permanent microscopic topographical features have also been developed (*23*). Because of their static nature, droplet motion on these surfaces cannot be controlled but is determined by gravity. In mechanowetting, however, the direction (and velocity) of droplet motion can be set or actively controlled so that water and debris can be collected at designated locations.

We emphasize that the only requirement for driving droplets by mechanowetting is a topographical deformation near the three-phase line to influence the balance of local surface tension, which can be achieved using our unidirectional mechanical traveling wave device, but its applicability is certainly not limited to that. If the used belt is able to rotate around the *z* axis, for instance, then the droplet will be able to move in a different direction in the current setup. However, the setup used has obvious limitations since it was specifically designed as an experimental proof-of-concept device for the mechanowetting mechanism. In further developments, responsive surface topographies that feature a mechanical deformation in response to external stimuli such as light (*24*), magnetic fields (*25*), and temperature (*26*) can be used. Light-responsive liquid crystal polymers and elastomers are especially attractive to create dynamic surface topographies because of their precise spatial-temporal control (*27*–*31*), enabling traveling surface undulations by structured (*32*) or moving (*21*) light sources or constant illumination assisted by self-shadowing (*33*). Moreover, droplet transport can also be induced through dynamic surface deformations that are different from traveling surface waves, allowing flexibility in design and omnidirectional droplet movement (see, e.g., the circular corrugations in fig. S7G). Applications that require controlled splitting and merging of droplets (*4*, *8*) could be achieved by creating a surface that consists of two traveling waves that travel toward (or away from) each other. All in all, we believe that mechanowetting, when fully explored, will open exciting new opportunities for high-precision droplet handling in a wide range of applications based on three-phase line manipulation by switchable surface topographies. Examples are microfluidics (diagnostics and cell handling and analysis), self-cleaning surfaces (medical devices, marine sensors, windows, and solar panels), and dew harvesting.

MATERIALS AND METHODS

Traveling wave device

The main functional part of the traveling wave device consists of a titanium conveyor belt with speed control, mounted in a vacuum chamber, which is shown in fig. S4A. The surface topography of the belt is shown in fig. S4B; it consists of an array of straight rounded ridges at a pitch of $\lambda = 500$ μm (see Fig. 1 for the definition of the system parameters). The belt was constructed using electrical discharge machining. The belt was wrapped tightly around two identical drums and driven by a motor to perform a conveying motion. The belt, motor, and drums were placed inside a chamber, which was made airtight. A 50-μm-thick PDMS film was made by spin-coating and fixed onto an aluminum frame, which was placed on top of the exposed part of the belt. By creating a low pressure inside the device, the PDMS film was pressed against the belt and followed its surface contour, i.e., a surface wave was formed (see Fig. 1 and fig. S4B). When the belt moved, a propagating transverse wave was then produced on the PDMS film, with the wavelength and the speed determined by the geometry and the speed of the belt, while the wave amplitude was controlled by the pressure level inside the chamber. On closer examination, each repeating section of the wave is composed of two half circles; however, the value of the wave amplitude is not the same at every location of the PDMS film, which is mainly caused by friction between the film and the belt (fig. S4C). These deviations from a perfect sinusoidal wave were measured and can be fitted to a theoretical model derived from the frictional stresses, as shown in fig. S4C and derived in fig. S8. When carrying out the climbing droplet experiments for different droplet sizes, the droplets were all placed at the same starting location to guarantee consistent wave amplitudes and improve reproducibility of the experiment. The experimentally measured wavelength, amplitude, and contact angle were used in the numerical simulations, described in more detail below.

PDMS film preparation

First, a layer of SU-8 2025 photoresist (MicroChem) was spin-coated onto a 100 mm wafer at 3000 rpm for 1 min. Then, after heating the wafer on a hot plate at 95°C for 2 min, a PDMS mixture at 12:1 (mass) ratio (base: curing agent; SYLGARD 184) was spin-coated on top of the SU-8 layer at 1200 rpm for 1 min. After curing the PDMS in an oven at 65°C for 2 hours, the film was released by immersing the wafer in a bath of mr-Dev 600 (micro resist technology). Then, the released film was transferred to a bath of toluene, which swells the film by 50%, and the film was quickly fixed afterward into an aluminum frame with a rubber O-shaped ring to retain the amount of swelling. Next, the film was washed using isopropanol and dried by nitrogen flow, which caused the film to shrink. The shrinking created a small amount of pretension that is needed to prevent wrinkling and folding of the PDMS when subjected to the frictional forces against the moving belt. Before placing the frame on the setup, a droplet of silicone oil with a viscosity of 5 mPa·s was placed in the middle of the film, which swells the middle part of the film, to reduce the pretension. Last, a lubrication oil (consisting of a mixture of W40 engine oil and the silicone oil) was applied on the belt to reduce friction and prevent tearing of the film. The process of mounting the PDMS film is shown in fig. S5.

Definition of the droplet size *d*

The diameter d of the solid-liquid interfacial area of the spherical cap-shaped droplet on a flat surface is given by

$$d = 2V^{\frac{1}{3}}\sin\,\theta_Y\left(\frac{\pi}{3}(2-3\,\cos\,\theta_Y+\cos^3\theta_Y)\right)^{-\frac{1}{3}} \quad (1)$$

where V is the droplet volume and θ_Y is the contact angle.

Mechanowetting experiments

In the climbing droplet experiments, a fluid mixture of 3:1 water-isopropanol in mass was used to make the droplets. The setup was fixed onto a stage that can be tilted at different angles with respect to the horizontal plane. Then, the belt was actuated to move at a linear speed of 0.57 mm s^{-1}, and the vacuum pump was set to have a pressure difference across the film of −0.1 bar. This pressure setting resulted in a wave geometry shown in fig. S4B and was measured to have a wave amplitude between 2 and 9 μm, depending on the location (fig. S4C). Then, a series of droplets of predetermined volumes were placed by hand using pipetting at the same location on the PDMS surface, ensuring a reproducible amplitude of $A = 4 \pm 1$ μm (emphasized by the marked area in fig. S4C). At incremental tilting angles of the setup, the critical angle at which the droplets can no longer be transported uphill was recorded, for the different droplet volumes used. For the "self-cleaning" experiment reported in Fig. 4D, we used calcium carbonate particles (<5 μm; Sigma-Aldrich) as a model for contaminating particles.

Measurement of wave amplitude

The measurement of the wave amplitude was done by using an interferometer (Sensofar) to directly image the PDMS film. The film was actuated for a significant amount of time before the measurement to obtain the wave amplitude difference along the wave direction. Figure S4C shows the result of such measurements, in which the gradual change of wave amplitude along the surface of the PDMS film is visible. The measurement was done using the same conditions as the climbing droplet experiments, as described above.

The wave amplitude ranges from approximately 2 μm at the left of the PDMS film to about 8 μm at the right (note that the belt and, therefore, also the wave run from left to right). The result shows good agreement with the theoretical model that is explained in fig. S8, when we assume a friction coefficient of 0.8.

Contact angle measurements

The contact angles of the droplets on the PDMS films were measured using a setup built in-house and processed using ImageJ software with the "contact angle" plug-in. We measured both the advancing and receding contact angles of droplets consisting of varying water-isopropanol mixtures, placed on both a virgin PDMS film after it was fixed onto the metal frame and on the same film 5 min after applying a small amount of silicone oil (5 mPa·s) on the bottom side of the film. The results can be found in fig. S4 (D and E). In the main mechanowetting experiments presented in Fig. 2A, a fluid mixture of 3:1 water-isopropanol in weight was used.

From the results of the contact angle measurement, we can see that with silicone oil lubrication (which is close to the condition during the mechanowetting experiments), the contact angle hysteresis is significantly reduced, while the mean contact angle is not changed significantly. This is beneficial for moving the droplets on the traveling wave device, as too large hysteresis can counteract the driving effect from the surface geometry. Note that we used a lubrication oil consisting of engine oil and low-viscosity silicone oil between the film and the belt, so we expect contact angles very similar to those shown in fig. S4E in our experiments. In the mechanowetting experiments, we used a fluid mixture of 3:1 water-isopropanol in volume for which, as can be seen in fig. S4E, the advancing and receding contact angles are 68°, which is the value used in the numerical simulations.

Computational fluid dynamics

The numerical modeling was conducted within the OpenFOAM 2.3.1 framework (*34*). To model capillary effects, we computationally solved the Navier-Stokes and continuity equations, supplemented by the two-phase volume-of-fluid formulation with the continuous surface tension force (CSF) method (*15*). We modified the CSF formulation by calculating the surface tension effects based on a smoothed indicator function to partially eliminate spurious currents and accurately model millimeter-sized droplets (*16*). The dynamic surface topography was modeled using deformation of the mesh boundary. This was done by prescribing a vertical displacement function to the boundary points of the mesh and updating the rest of the mesh points according to a diffusion method to guarantee sufficient mesh quality. The prescribed displacement function mimics the traveling wave surface topography used in the experiments by fitting the (periodic) instantaneous experimental geometry by two circular arcs. The tilting angle of the experimental setup was modeled by slowly rotating the gravitational acceleration vector during the simulations.

SUPPLEMENTARY MATERIALS

Supplementary material for this article is available at http://advances.sciencemag.org/cgi/content/full/5/6/eaaw0914/DC1

Supplementary Text
Fig. S1. Tracer particle path lines.
Fig. S2. Theory, CFD, and experiments.
Fig. S3-I. Theoretical dynamic pinning number dependences.
Fig. S3-II. Theoretical dynamic pinning number dependencies.
Fig. S4. Traveling wave device and contact angle measurements.
Fig. S5. Application of the PDMS film on the traveling wave device.
Fig. S6. Mechanowetting mechanism schematics.
Fig. S7. Dynamic pinning theory of multiple surface structures.
Fig. S8. Schematic of the symbols used in the model for calculating the wave amplitude.
Movie S1. Transport of a droplet with tracer particles.
Movie S2. Simulation of the droplet transport.
Movie S3. Two-droplet experiment.
Movie S4. Vertical transport.
Movie S5. Ceiling transport.
Movie S6. Mass transport of multidispersed droplets.
Movie S7. Self-cleaning surface.
Reference (*35*, *36*)

REFERENCES AND NOTES

1. B. Wang, Y. Zhang, L. Shi, J. Li, Z. Guo, Advances in the theory of superhydrophobic surfaces. *J. Mater. Chem.* **22**, 20112–20127 (2012).
2. D. R. Reyes, D. Iossifidis, P.-A. Auroux, A. Manz, Micro total analysis systems. 1. Introduction, theory, and technology. *Anal. Chem.* **74**, 2623–2636 (2002).
3. G. M. Whitesides, The origins and the future of microfluidics. *Nature* **442**, 368–373 (2006).
4. H. Song, D. L. Chen, R. F. Ismagilov, Reactions in droplets in microfluidic channels. *Angew. Chem. Int. Ed.* **45**, 7336–7356 (2006).
5. M. T. Guo, A. Rotem, J. A. Heyman, D. A. Weitz, Droplet microfluidics for high-throughput biological assays. *Lab Chip* **12**, 2146–2155 (2012).
6. Y.-Y. Lin, E. R. F. Welch, R. B. Fair, Low voltage picoliter droplet manipulation utilizing electrowetting-on-dielectric platforms. *Sens. Actuators B Chem.* **173**, 338–345 (2012).

7. V. Srinivasan, V. K. Pamula, R. B. Fair, An integrated digital microfluidic lab-on-a-chip for clinical diagnostics on human physiological fluids. *Lab Chip* **4**, 310–315 (2004).
8. S. K. Cho, H. Moon, C.-J. Kim, Creating, transporting, cutting, and merging liquid droplets by electrowetting-based actuation for digital microfluidic circuits. *J. Microelectromech. Syst.* **12**, 70–80 (2003).
9. A. Hashmi, Y. Xu, B. Coder, P. A. Osborne, J. Spafford, G. E. Michael, G. Yu, J. Xu, Leidenfrost levitation: Beyond droplets. *Sci. Rep.* **2**, 797 (2012).
10. H. Linke, B. J. Alemán, L. D. Melling, M. J. Taormina, M. J. Francis, C. C. Dow-Hygelund, V. Narayanan, R. P. Taylor, A. Stout, Self-propelled Leidenfrost droplets. *Phys. Rev. Lett.* **96**, 154502 (2006).
11. J. Berná, D. A. Leigh, M. Lubomska, S. M. Mendoza, E. Pérez, P. Rudolf, G. Teobaldi, F. Zerbetto, Macroscopic transport by synthetic molecular machines. *Nat. Mater.* **4**, 704–710 (2005).
12. A. Wixforth, Acoustically driven planar microfluidics. *Superlattices Microstruct.* **33**, 389–396 (2003).
13. L. Y. Yeo, J. R. Friend, Ultrafast microfluidics using surface acoustic waves. *Biomicrofluidics* **3**, 012002 (2009).
14. T.-D. Luong, N.-T. Nguyen, Surface acoustic wave driven microfluidics – A review. *Micro Nanosyst.* **2**, 217–225 (2010).
15. C. Liu, J. Li, C. Xiang, L. Che, Z. Wang, X. Zhou, Long-range spontaneous droplet self-propulsion on wettability gradient surfaces. *Sci. Rep.* **7**, 7552 (2017).
16. H. G. Weller, G. Tabor, H. Jasak, C. Fureby, A tensorial approach to computational continuum mechanics using object-oriented techniques. *Comput. Phys.* **12**, 620 (1998).
17. C. W. Hirt, B. D. Nichols, Volume of fluid (VOF) method for the dynamics of free boundaries. *J. Comput. Phys.* **39**, 201–225 (1981).
18. J. U. Brackbill, D. B. Kothe, C. Zemach, A continuum method for modeling surface tension. *J. Comput. Phys.* **100**, 335–354 (1992).
19. E. Berberović, N. P. van Hinsberg, S. Jakirlić, I. V. Roisman, C. Tropea, Drop impact onto a liquid layer of finite thickness: Dynamics of the cavity evolution. *Phys. Rev. E* **79**, 036306 (2009).
20. A. Q. Raeini, M. J. Blunt, B. Bijeljic, Modelling two-phase flow in porous media at the pore scale using the volume-of-fluid method. *J. Comput. Phys.* **231**, 5653–5668 (2012).
21. J.-a. Lv, Y. Liu, J. Wei, E. Chen, L. Qin, Y. Yu, Photocontrol of fluid slugs in liquid crystal polymer microactuators. *Nature* **537**, 179–184 (2016).
22. M. K. Chaudhury, G. M. Whitesides, How to make water run uphill. *Science* **256**, 1539–1541 (1992).
23. R. Blossey, Self-cleaning surfaces – Virtual realities. *Nat. Mater.* **2**, 301–306 (2003).
24. T. J. White, D. J. Broer, Programmable and adaptive mechanics with liquid crystal polymer networks and elastomers. *Nat. Mater.* **14**, 1087–1098 (2015).
25. Y. Huang, B. B. Stogin, N. Sun, J. Wang, S. Yang, T.-S. Wong, A switchable cross-species liquid repellent surface. *Adv. Mater.* **29**, 1604641 (2017).
26. C. Ohm, M. Brehmer, R. Zentel, Liquid crystalline elastomers as actuators and sensors. *Adv. Mater.* **22**, 3366–3387 (2016).
27. G. Van der Veen, W. Prins, Photomechanical energy conversion in a polymer membrane. *Nat. Phys. Sci.* **230**, 70–72 (1971).
28. T. Ikeda, M. Nakano, Y. Yu, O. Tsutsumi, A. Kanazawa, Anisotropic bending and unbending behavior of azobenzene liquid-crystalline gels by light exposure. *Adv. Mater.* **15**, 201–205 (2003).
29. D. Liu, L. Liu, P. R. Onck, D. J. Broer, Reverse switching of surface roughness in a self-organized polydomain liquid crystal coating. *Proc. Natl. Acad. Sci. U.S.A.* **112**, 3880–3885 (2015).
30. L. Liu, P. R. Onck, Enhanced deformation of azobenzene-modified liquid crystal polymers under dual wavelength exposure: A photophysical model. *Phys. Rev. Lett.* **119**, 057801 (2017).
31. D. Liu, C. W. M. Bastiaansen, J. M. J. den Toonder, D. J. Broer, Photo-switchable surface topologies in chiral nematic coatings. *Angew. Chem. Int. Ed.* **51**, 892–896 (2012).
32. S. Palagi, A. G. Mark, S. Y. Reigh, K. Melde, T. Qiu, H. Zeng, C. Parmeggiani, D. Martella, A. Sanchez-Castillo, N. Kapernaum, F. Giesselmann, D. S. Wiersma, E. Lauga, P. Fischer, Structured light enables biomimetic swimming and versatile locomotion of photoresponsive soft microrobots. *Nat. Mater.* **15**, 647–653 (2016).
33. A. H. Gelebart, D. J. Mulder, M. Varga, A. Konya, G. Vantomme, E. W. Meijer, R. L. B. Selinger, D. J. Broer, Making waves in a photoactive polymer film. *Nature* **546**, 632–636 (2017).
34. The OpenFOAM Foundation (2004); www.openfoam.org.
35. T. Young, An essay on the cohesion of fluids. *Philos. Trans. R. Soc. London* **95**, 65–87 (1805).
36. J. F. Joanny, P. G. de Gennes, A model for contact angle hysteresis. *J. Chem. Phys.* **81**, 552–562 (1984).

Acknowledgments: We thank the Equipment and Prototype Center of TU Eindhoven for building the traveling wave device, E. H. Eggels for assistance in the experiments, and K. Hendriks and L. Liu for fruitful discussions. **Funding:** This work was supported by NWO-TTW under project number 12826, "Dynaclean." **Author contributions:** E.D.J. developed the numerical and theoretical models and performed the simulations. Y.W. designed and built the device and performed the climbing droplet experiments. J.M.J.D.T. and P.R.O. designed the research. E.D.J. and P.R.O. wrote the manuscript. **Competing interests:** The authors declare that they have no competing interests. **Data and materials availability:** All data needed to evaluate the conclusions in the paper are present in the paper and/or the Supplementary Materials. Additional data related to this paper and codes may be requested from the authors.

Submitted 16 November 2018
Accepted 7 May 2019
Published 14 June 2019
10.1126/sciadv.aaw0914

Citation: E. De Jong, Y. Wang, J. M. J. Den Toonder, P. R. Onck, Climbing droplets driven by mechanowetting on transverse waves. *Sci. Adv.* **5**, eaaw0914 (2019).